RSC Advances

PAPER

View Article Online
View Journal | View Issue

Cite this: *RSC Adv.*, 2024, **14**, 19806

Direction-oriented fiber guiding with a tunable tri-layer-3D scaffold for periodontal regeneration†

Sarin Abraham,[a] Pallavi Gupta,[a] Kavitha Govarthanan,[b] Suresh Rao [a] and Tuhin Subhra Santra *[a]

Received 25th February 2024
Accepted 30th May 2024

DOI: 10.1039/d4ra01459f

rsc.li/rsc-advances

Multilayered scaffolds mimicking mechanical and biological host tissue architectures are the current prerequisites for successful tissue regeneration. We propose our tunable tri-layered scaffold, designed to represent the native periodontium for potential regenerative applications. The fused deposition modeling platform is used to fabricate the novel movable three-layered polylactic acid scaffold mimicking *in vivo* cementum, periodontal ligament, and alveolar bone layers. The scaffold is further provided with multiple angulated fibers, offering directional guidance and facilitating the anchorage dependence on cell adhesion. Additionally, surface modifications of the scaffold were made by incorporating coatings like collagen and different concentrations of gelatin methacryloyl to enrich the cell adhesion and proliferation. The surface characterization of our designed scaffolds was performed using tribological studies, atomic force microscopy, contact angle measurement, scanning electron microscopy, and micro-computed tomography. Furthermore, the material characterization of this scaffold was investigated by attenuated total reflectance-Fourier transformed infrared spectroscopy. The scaffold's mechanical characterization, such as strength and compression modulus, was demonstrated by compression testing. The L929 mouse fibroblast cells and MG63 human osteosarcoma cells have been cultured on the scaffold. The scaffold's superior biocompatibility was evaluated using fluorescence dye with fluorescence microscopy, scanning electron microscopy, *in vitro* wound healing assay, MTT assay, and flow cytometry. The mineralization capability of the scaffolds was also studied. In conclusion, our study demonstrated the construction of a multilayered movable scaffold, which is highly biocompatible and most suitable for various downstream applications such as periodontium and *in situ* tissue regeneration of complex, multilayered tissues.

1 Introduction

The tooth is supported by periodontium, which is made of two hard structures, bone and cementum, and connected by fibers called the periodontal ligament, a soft structure running at different angles.[1] It is a unique structure constituted by the fibers anchored into the two hard tissues, which helps to withstand masticatory forces.[1] Biofilms formed on the oral tissues induce inflammation (periodontitis), an irreversible disease that compromises the supporting tissues.[2] This is the most prevalent oral disease globally, and if left untreated, it will lead to the loss of tooth/teeth.[3] Periodontitis is the source of infection/inflammation that can metastasize to different organs and hence is a risk factor for cardiovascular disease, diabetes mellitus, preterm low birth, rheumatoid arthritis, and a host of other diseases.[4] Hence, it is very critical that the condition is arrested and desirably reversed to its original structure and function.

Major obstacles to periodontal healing that result in hampered regeneration include the role of more than 500 species of oral microorganisms, conventionally non-regenerating periodontal tissues after eliminating the disease, and the constant, cyclic biting forces that are impossible to avoid and prevent the body from mending.[4] The prognosis has been enhanced by improvements in prevention and treatment choices but preventing tissue loss and ensuring the best possible tissue regeneration have been difficult for decades.[5] There has been a paradigm shift in the treatment of periodontitis from conventional scaling, root planning, and radical surgery.[6] The past few decades have seen regenerative procedures such as guided tissue regeneration, bone grafts, and incorporation of growth factors.[7] Since tissue engineering came into vogue, stem cells and scaffolds have gained attention.[6]

Sowmya *et al.* showed how to regenerate the different layers of the periodontium using a combination of hydrogel, nanoparticles, and growth factors.[8] However, various angulations of

---

[a] Department of Engineering Design, Indian Institute of Technology Madras, Chennai 600036, India. E-mail: tuhin@iitm.ac.in; santra.tuhin@gmail.com

[b] Institute for Stem Cell Science and Regenerative Medicine (DBT-inStem), Bengaluru, Karnataka 560065, India

† Electronic supplementary information (ESI) available. See DOI: https://doi.org/10.1039/d4ra01459f

the periodontal ligaments have not been demonstrated. Ding *et al.* demonstrated the sequential release of basic fibroblast growth factor and bone morphogenetic protein-2 to regenerate cementum, periodontal ligament, and bone.[9] However, the framework does not imitate periodontal anatomy and does not enable compartmentalization or the necessary anchoring between the layers. Vurat *et al.* aimed to create a preclinical model that mimics the interaction between the periodontal ligament and bone *via* bioprinting of scaffolds.[10] Although, the model falls short of accurately depicting the periodontal structure.

A monophasic chitosan–hyaluronic acid hydrogel scaffold for periodontal regeneration has been suggested by Miranda *et al.*[11] Improved cellular viability and strong CD44 expression were demonstrated using the scaffold.[11] However, it did not offer cell compartmentalization or a means of securing the ligament to the bone or cementum. Guo *et al.* proposed a double-layered scaffold of silk fibroin film and porous silk fibroin nanohydroxyapatite.[12] Still, they failed to mimic the tri-layered structure. Sowmya *et al.* established how to regenerate the layers of the periodontium complex utilising a tri-layered scaffold that contains different growth factors.[8] Even so, the information regarding the angulation of ligaments and anchorage has not been emphasized. Histological evidence of regeneration is evident in these scaffolds but not in the architecture. Moreover, many of these scaffolds have not faced clinical trials. This is crucial since no surgically treated teeth are kept from functioning, unlike a limb fracture. All the treated teeth undergo masticatory function within 24 hours after surgery, which will have major implications on the healing tissues and the scaffold. Since some scaffolds, such as cell sheets and hydrogels, are not stiff, it is important to comprehend how occlusal forces affect them.[13]

Many drawbacks of old primitive scaffolds have been overcome in the recent 3D printed, cell-sheet, or multiphasic scaffolds.[13] Yet, a few specific requirements, such as architecture, anchorage, and angulation of fibers that are required to get an ideal regeneration, have not been addressed.[14] Layer-by-layer printing of a composite material made of polycaprolactone (PCL) and hydroxyapatite (HA) is proposed by Lee *et al.*[15] However, the anchoring between the ligament, bone, and cementum has not been addressed. Yao *et al.* demonstrated how to regenerate the bone layer, the interface between the bone and the periodontal ligament, and the periodontal ligament using the melt electrowriting approach.[16] But the tri-layered periodontium structure has not been modeled. Moreover, in the above-mentioned scaffolds, unless protected on the top portion by collagen membrane, there is a high probability of epithelium migrating down onto the root surface, compromising regeneration.[17] Also, though histological scaffolds have demonstrated cementum, periodontal ligament, and bone regeneration, the formation of Sharpey's fibers and the multi-angular orientation of periodontal fibers are not evident.[13]

One of the commonly used biomaterials in periodontal regeneration is collagen. The primary factors contributing to this are its biocompatibility, bioactivity, and similarity to the extracellular matrix (ECM) found in periodontal tissues. However, they must be reinforced to attain the required mechanical properties to withstand the masticatory forces,[2] and attaining the required angulation of the periodontal ligament is difficult. Polycaprolactone (PCL),[15,18] polylactic acid (PLA),[19] and poly(lactic-*co*-glycolic acid) (PLGA)[8] have attracted many researchers due to their biocompatibility, tunable degradation kinetics, drug delivery carriers, biodegradation, and compatible mechanical properties, but they have longer degradation time and do not provide the required bioactivity. Hence, these polymer materials should be reinforced with a hydrogel which could offer the possibility of mimicking the biological and mechanical microenvironments of human tissue.[20] Researchers have tried to use 3D printing technology to mimic the periodontal structure, but they have not provided the angular channels to form the periodontal ligament.[20] Hydroxyapatite[21] and tricalcium phosphate (TCP)[22] are also popular because they mimic the mineral composition of natural bone, and their osteoconductive properties promote bone formation, but they are brittle and fabricating scaffolds with controlled microstructure, porosity, and mechanical properties can be challenging.[22] Gelatin scaffolds can encapsulate cells and bioactive molecules, facilitating their controlled release and enhancing periodontal tissue regeneration.[21] However, these scaffolds do not possess the required mechanical properties to withstand the masticatory forces.[23]

Considering the intricate spatiotemporal periodontal structure and the necessity for rapid prototyping, the selection of the appropriate biomaterial becomes crucial to guarantee that the scaffold aligns accurately to promote optimal regeneration.[24] Also, providing appropriate mechanical strength, tunable degradation kinetics, bioactivity, and compatibility with specific cell types has to be addressed. Based on the above observations and the advantages of reinforcing PLA with hydrogel, we consider PLA as the material for the scaffold in our present study.

Ensuring proper cellular directionality and fiber orientation is crucial for periodontal regeneration.[25] Cell alignment and directional position would facilitate accelerated regeneration. The pores in the angulated tubes in our proposed design will facilitate the cells to migrate and synthesize collagen in the desired direction due to the angulation of tubes. The collagen fibers in developing teeth are mostly one-directional. As the tooth contacts the opposite tooth, the occlusal function in multiple directions will lead to the bundling of collagen fibers in different directions to withstand multidirectional forces. However, after periodontal regenerative surgery, the tooth still in a functional position may prevent the fiber from bundling due to the constant load on developing fibers. So, there is a chance that fibers may struggle to orient themselves in various angles. This will be a major issue in a clinical situation that has not been addressed so far. By providing PLA hollow tubes as in our work, the cells, and the regenerating fibers will be protected from occlusal load and get anchored unhindered. This angulation and anchorage of the periodontal ligament to the bone and cementum layers helps to stabilize the tooth in place and helps to withstand the constant masticatory forces.

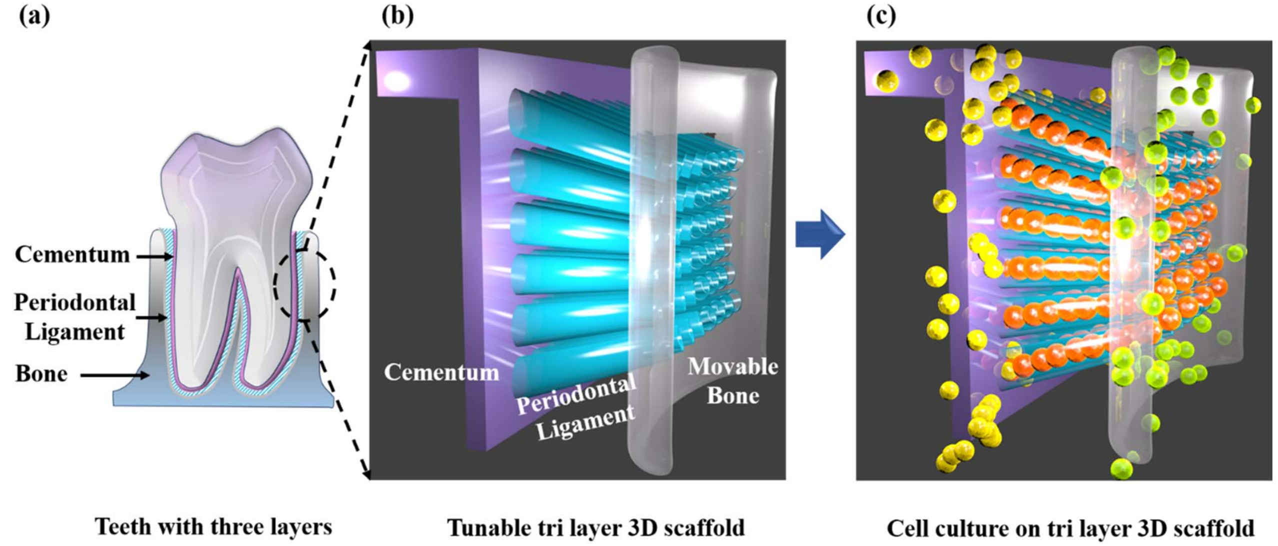

Fig. 1 Schematic of direction-oriented fiber guiding with tunable tri-layer-3D scaffold (a) teeth with three layers (b) fabricated direction-oriented fiber guiding with tunable tri layer -3D scaffold (c) cell culture on direction-oriented fiber guiding tri layer 3D scaffold.

An ideal periodontal regeneration includes the regeneration of all three tissues (bone, cementum, periodontal ligament) in the accurate ratio to the original position and, most importantly, gaining the original architecture. In the process of achieving ideal regeneration, there are obstacles like an infection that needs to be controlled and need to create an idealistic environment for the cells to "feel at home." Unlike any other tissue or organ, the periodontium is under constant threat of functional (masticatory) cyclic forces exerting pressure on the healing tissues. The most important criterion is the anchorage of fibers, which requires a highly coordinated tissue regeneration in a spatiotemporal manner. However, none of the scaffolds presently developed provide a spatiotemporal tissue regeneration.

Understanding the factors influencing cell adhesion, proliferation, and cell viability is essential for ideal periodontal regeneration using scaffolds. One approach to investigating these factors is through hypothesis testing, wherein the null hypothesis (H0) posits that there are no significant differences or relationships between the various coating and potential tissue regeneration. In the context of this study, we aim to explore the impact of various coatings on PLA scaffolds for periodontal tissue regeneration. Specifically, we hypothesize that our unique design, along with the surface modification, has a statistically significant effect on the regenerative capability using the scaffold.

While previous studies have provided valuable insights into various design aspects gaps remain in our understanding of creating individual compartments for each tissue, running angulated tubes for specific fiber bundle orientation, and providing anchorage between hard and soft tissues. In addition to the above, the incorporation of shelves to prevent epithelium from migrating down onto the root surface and providing a provision for gingival fibroblast cells to migrate (the tissue presents above the three periodontal layers) into the hollow tubes to form fibers at the earliest need to be addressed. By examining the null hypothesis and its potential rejection, we seek to contribute to the current body of knowledge by elucidating the relationship between the various surface coatings and periodontal regeneration.

Taking into consideration the above-mentioned lacunae in scaffold designing, we have made a prototype of a guiding scaffold, as shown in Fig. 1. Here, we have fabricated and characterized an angulated direction-oriented tunable three-dimensional scaffold that meets almost all the above necessary conditions for perfect regeneration. In order to build a tri-layered 3D-printed scaffold for periodontal regeneration with potential customising options for unique therapeutic effects, we used the 3D-printing platform to generate the PLA scaffold. Our unique design imitates the three layers of cementum, periodontal ligament, and alveolar bone, making it easier to provide the two hard tissues with the necessary anchorage and directing ligament growth in the right directions. The scaffold's two-part construction makes it simple to fit into the periodontal defect no matter how the surgical defect is shaped. In contrast to other scaffolds, it compartmentalises hard tissue and permits the direct injection of endogenous cells or growth hormones.

2 Materials and methods

2.1 Materials

The polylactic acid (PLA) filament (1.75 mm, white colour) was bought from WOL 3D. Collagen from Calf skin (CAS 9007-34-5), gelatin type A, 300 bloom from porcine skin (cat. no. G2500), methacrylic anhydride (MA) (cat. no. 276685), phthaldialdehyde reagent solution (cat. no. P0532), ascorbic acid (cat. no. 50-81-7), dexamethasone (cat. no. D4902), β-glycerophosphate disodium salt hydrate (cat. no. G9422) and 1,1,1,3,3,3 hexamethyldisilazane (cat. no. 999-97-3) (HMDS) were purchased from Sigma Aldrich.

The lithium acyl phosphinate (LAP) was purchased from TCI Chemical (cat. no. L0290). Dialysis membrane (cat. no. LA395), phosphate buffered saline (PBS) 10X (cat. no. ML023), and Alizarin Red S (cat. no. GRM894) was purchased from HiMedia. The Dulbecco's Modified Eagle Medium DMEM (cat. no. 12100046), penicillin–streptomycin (cat. no. 15140148), fetal bovine serum (FBS) (cat. no. 10270106) and non-essential amino acid (cat. no. 11140050) were purchased from Gibco.

Calcein AM (cat. no. C3099) and propidium iodide (cat. no. 32042090) were purchased from Invitrogen. We also procured distilled water, polyethersulfone (PES) membrane syringe filter with (0.2 μm pore size), and antibiotic-antimycotic (100X) (Gibco, cat. no. 15240062).

2.2 Fabrication of scaffold

The fused deposition modeling (FDM) technique was utilized to generate the three-layered scaffold. First, using Creo Parametric 8.0.4.0, a computer-aided modeling (CAD) of the constituent components was made. The various parts were afterward joined at the required angulation to produce the final tri-layered structure. The model was sliced employing FlashPrint 5.5.2 software after optimisation. A FLASHFORGE Creator 3 FDM printer with a 0.4 mm nozzle diameter was utilized to print the scaffold. The platform temperature was set to 60 °C, the extrude temperature to 200 °C, and an infill density of 100% were the printing parameters used to print the 3D scaffold. The three-layered scaffold is made up of a first layer (representing the cementum), the second layer consists of the angular tubes (representing the periodontal ligament), and the third layer (representing the bone) with continuous slots that slide over the opposite end of the angular tubes of the first cementum layer. The periodontal ligament has wide pores on its surface to allow cells to migrate into the tubes and populate. The dimensions of the printed scaffolds are cementum (12 mm × 12 mm × 0.6 mm), bone (13 mm × 12 mm × 0.6 mm), periodontal ligament length of 4 mm, exterior diameter of 2 mm, and inner diameter of 1.6 mm. The 3D-printed, direction-oriented, tunable scaffold is named PLA. This uncoated PLA scaffold will be the control. Fig. 2(a) summarizes the scaffold fabrication steps used for the study. Fig. 2(b) illustrates the optical image of the fabricated direction-oriented tunable scaffold where angulated ligament fiber is anchored between cementum and bone. Fig. 2(c) demonstrates the surface topography of the fabricated cementum layer with the attached ligaments.

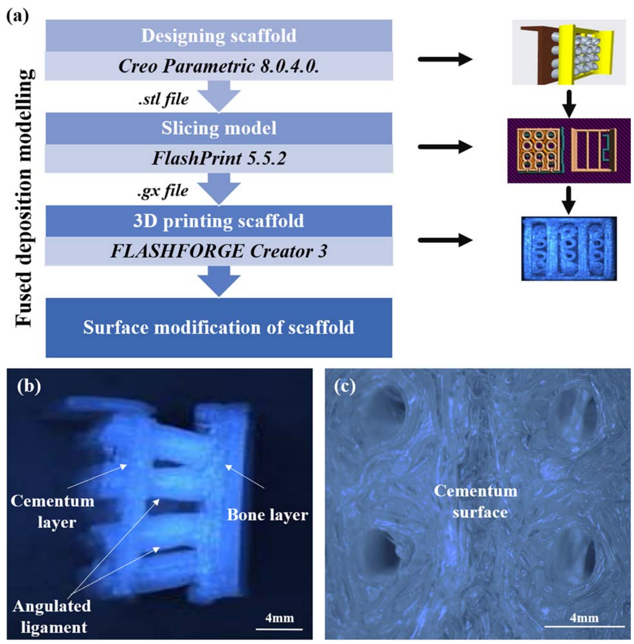

Fig. 2 (a) Schematic depicting the scaffold fabrication steps (b) optical images of the fabricated direction oriented tunable scaffold, where angulated ligament fiber is anchored between cementum and bone (c) optical image of the surface of cementum layer anchored with ligament.

2.3 Synthesis of GelMA

Methacrylated gelatin was synthesized as described previously in the literature.[26] Briefly, type A porcine skin gelatin 10% (w/v) was mixed into distilled water at 50 °C and stirred for an hour. Then, MA was dropped at a rate of 0.5 mL min^{-1} to the gelatin solution under stirring with 240 rpm at 50 °C and allowed to react for three hours. Preheated distilled water at 40 °C is added to stop the reaction. The solution is then dialyzed against distilled water using 12 k to 14 kDa cutoff dialysis tubing at 40 °C under stirring conditions at 500 rpm. The water was changed twice a day for one week. The solution is filtered and stored in falcon tubes and then stored at −80 °C overnight. Finally, the solution was lyophilized for one week to generate a porous white foam and stored at −20 °C until further use.

2.4 GelMA solution preparation

The photoinitiator LAP was used as it helps in the photo-polymerization process and is less toxic than other photo-initiators.[27,28] The LAP was dissolved in PBS while stirring at 500 rpm for ten minutes at 60 °C. It was filtered using a sterilized syringe filter. Then, lyophilized GelMA with concentrations of 5% (w/v) and 10% (w/v) was dissolved in the above solution and stirred for 30 minutes at 70 °C. The pH of the hydrogel solution was adjusted to 7.4. For the study, 5% (w/v) and 10% (w/v) GelMA concentrations were used to visualize the effect of L929 (mouse fibroblast cells) and MG63 (human osteosarcoma cells) on the surface-modified PLA scaffold. These concentrations have been chosen to enhance cell spreading and increase cell viability.[29]

2.5 Preparation of collagen coated PLA scaffold (PLA/COL)

The PLA scaffold was rinsed with distilled water thrice, and then ultraviolet (UV) light was treated overnight to remove the unbound contamination. The PLA scaffold was immersed in 0.5 mL of collagen with a working concentration of 0.66% (v/v). This scaffold is named PLA/COL and was used for further cell culture studies.

2.6 Preparation of 5% GelMA coated PLA scaffold (PLA/5 GelMA) and 10% GelMA coated PLA scaffold (PLA/10 GelMA)

After PLA scaffold is treated with UV light overnight, the PLA scaffolds were immersed in 5% (w/v) GelMA and 10% (w/v)

GelMA solution with 0.067% LAP and later photopolymerized for 3 minutes in UV cure (wavelength of 405 nm and light intensity of 90 W) setup and these scaffolds were named PLA/5 GelMA and PLA/10 GelMA respectively. It was washed with PBS followed by an immersion in 20% (v/v) antibiotic–antimycotic solution overnight. The scaffolds were once again washed with PBS and then used for cell culture studies.

2.7 Characterization of scaffold

The tri-layered direction-oriented tunable scaffold was imaged using micro-computed tomography (micro-CT) (GE Phoenix VTOMEX CT Scanner) to understand the microstructural details. The scan data for the PLA scaffold were collected using an X-ray tube setting of 80 kV, 100 μA, and an exposure period of 333 ms with a resolution of 27 nm. VGStudio Max 2.2.6 software was used to analyze the data.

Tribological study of the scaffold was carried out using R-tec MFT 5000 (USA), a multifunctional tribometer, to understand the coefficient of friction for the scaffolds. The coefficient of friction was determined using an Al_2O_3 ball with a diameter of 10 mm. The measurements were conducted for 30 minutes at 25 °C under a load of 2 N and at a velocity of 1 cm $second^{-1}$. The PLA scaffolds were used as such for the experiment. For the PLA/COL, PLA/5 GelMA, and PLA/10 GelMA, the samples were coated as mentioned in Sections 2.5 and 2.6. Further, the scaffolds were dried at room temperature.

The samples were subjected to Attenuated Total Reflectance-Fourier Transformed Infrared Spectroscopy (ATR FTIR) to analyze the functional groups present in the scaffold and to characterize the nature of chemical interaction. The samples were scanned using BRUNKER RFS 27- a standalone unit in the range of 4000 cm^{-1} to 400 cm^{-1} at room temperature.

Surface characterization was performed using atomic force microscopy (AFM) in tapping mode (Bruker's Dimension Icon). The scan area was set to 30 μm × 30 μm and kept constant for all the samples. Root mean square roughness (R_q) and average roughness (R_a) were measured after the images were flattened. NanoScope Analysis software was used for analysis. The cantilever material had a 0.01–0.025 ohm-cm Antimony(n) doped Silicon.

Scanning electron microscopy (SEM) (SNE-4500M high-resolution table-top) was used to study the surface morphology of the scaffold. The accelerated voltage was 30 kV with an emission current of 120 μA in high vacuum conditions.

Contact angle measurement was performed using Apex Acam-D3 goniometer. 4 μl of de-ionized (DI) water was placed carefully at atleast 3 different positions of the scaffold, and the contact angle was measured immediately at room temperature.

Compression tests are conducted by loading the test specimen between two plates and then applying a force to the specimen by moving the crossheads together. During the test, the specimen is compressed, and deformation *versus* the applied load is recorded. The compression test for the samples was conducted using Kudale instrument PC 2000 with a load cell of 2010 N. The rate of compression was set at 5 mm min^{-1}. Compressive strength at yield was determined from the first point on the stress–strain curve, at which an increase in strain was observed without an increase in stress.[30]

The methacrylation and the degree of functionalization (DoF) of GelMA were determined by proton nuclear magnetic resonance (^1H NMR) spectroscopy (Bruker Advance 400 MHz spectrometer). Proton signals at 2.9 ppm (protons of the methylene group of lysine) for the gelatin and GelMA were compared to determine the DoF.[31] The plot of ^1H NMR of gelatin and GelMA is provided in ESI Fig. S1.† The DoF was also verified using the fluoraldehyde assay.[32] The calibration curve for the fluoraldehyde assay is provided in ESI as Fig. S2.†

2.8 Cell culture and cell viability test

For the experiments, mouse fibroblast cell lines (L929) and osteoblast-like cell lines (MG63) were used and procured from the National Centre for Cell Science, Pune, India. L929 and MG63 cells were cultured using DMEM media and supplemented with 10% FBS, 1% amino acids, and 1% penicillin–streptomycin. Once the cells attained confluency, they were trypsinized and seeded onto the scaffolds to carry out further studies. The L929 cells were seeded on the cementum and ligament layers, and the MG63 cells were seeded on the bone layer. Calcein AM and propidium iodide (PI) dye were employed to stain the live and dead cells, respectively.[33] The PI dye can stain the nucleus of the dead cell and produce a red fluorescence color. The calcein AM can hydrolysis inside the cell and produce a green fluorescence color in live cell cytosol.

To visualize cell viability and biocompatibility tests on the 3D printed tunable scaffold, cells were briefly cultured on a scaffold using appropriate cell culture media. Then, 30 μl of calcein AM 3% (v/v) concentration was added and incubated for 10 min. Following the incubation, 10 μl of PI dye with a concentration of 1.5% (v/v) was added to the scaffold and incubated for 3 minutes.[34] Then, the images were subsequently captured with a fluorescent microscope (IX 73, Olympus, Japan) after 24 hours of growth, and the images were processed using ImageJ software. Additionally, MG63 and L929 cells were investigated by flow cytometry (BD FACS CANTO II, New Jersey, USA) to validate the count of dead and alive cells. The flow cytometry analysis was interpreted using the program FlowJo_v10.8.[34] Furthermore, cell viability was also assessed by MTT [3-(4,5-dimethylthiazol-2-yl)-2,5-diphenyl-2*H*-tetrazolium bromide] assay.[33]

2.9 Mineralization on the bone scaffold

Mineralization capability on the bone scaffold was examined using MG63 cell lines.[35] The scaffolds were seeded with cells and were cultured in DMEM and osteogenic media for 7 days. The osteogenic media was constituted using DMEM, 10% FBS, 1% penicillin/streptomycin, 10 nM dexamethasone, 50 μg mL^{-1} ascorbic acid, and 10 mM β-glycerophosphate.[35] After 7 days, the mineralized matrix was analysed using an Alizarin Red S staining method. After being cultured for 7 days the cells on the scaffold were washed with PBS and fixed in 4% paraformaldehyde for 15 min at room temperature. Then, images were captured using a microscope (Nikon Research Microscope

Model LV 100ND) equipped with a digital camera. To quantify matrix mineralization, each stained specimen was eluted in 10% acetic acid solution for 30 min at room temperature under mild shaking conditions.[36] The absorbance of Alizarin Red S extracts was measured at 405 nm using a Synergy H1 microplate reader. The data were the mean of three independent measurements.

2.10 SEM images of cell-cultured on scaffold

L929 cell lines were seeded on PLA, PLA/COL, PLA/5 GelMA, and PLA/10 GelMA scaffolds. The cells were allowed to grow for 48 hours on the scaffold and later fixed with 2.5% glutaraldehyde for 2 hours. Then, the scaffolds were rinsed with PBS for 10 minutes and then followed by washing with DI water. The samples were dried using incremental ethanol concentration from 35% to 100%, with each wash duration of 15 minutes. Subsequently, HMDS was used for the final washing of the scaffolds.[37] The samples were further vacuum-dried for 3 days and then imaged using a Carl ZEISS EVO 18-Germany scanning electron microscope after sputter coating with gold.

2.11 *In vitro* wound healing assay

L929 cells were grown in six-well plates until they reached 100% confluency. A small linear scratch was created in the confluent monolayer by gently scraping with a 200 μl micropipette tip. Subsequently, the culture medium was aspirated, and cells were washed with PBS in order to remove cell debris. Sterilized scaffolds were placed in all wells and incubated for 72 hours after adding 2 mL of serum-free medium per well. Cell migration was observed through an inverted microscope (Olympus IX 73 microscope with Qimaging MP3.3 camera). The cell culture wells were imaged at 0, 12, 24, 48 h, and 72 hours' time points, and the wound closure area between wound edges was calculated using ImageJ software.[38]

2.12 Statistical analysis

Each experiment was performed in triplicate, and the data obtained are reported as mean ± standard error of mean. Statistical analysis was done using two-way ANOVA test. Tukey's test was used for comparison among groups ($^{*}p < 0.0332$, $^{**}p < 0.0021$, $^{***}p < 0.0002$, and $^{****}p < 0.0001$). These were performed using GraphPad Prism 10.2.3.

3 Results and discussion

3.1 Structural and tribological characterization

Fig. 3 depicts the 3D model of the tri-layered scaffold. Fig. 3(a) shows an isometric view of the tri-layered scaffold. The grey tubes are the periodontal ligament guiding tubes which are attached to the brown cementum layer, and the yellow structure is the movable bone layer. Vertical layers (cementum and bone), made in two parts, facilitate fitting regardless of the shape of the surgical defect. They compartmentalize hard tissue areas, allowing endogenous cells to be directed into specific areas. This compartmentalization is unique to vertical layers, unlike other types that have overlapping phases. The cementum layer has angulated hollow tubes, allowing an early population of fibroblasts to form bundles. This unique design allows fiber bundles to grow into hard tissue space, allowing anchorage and

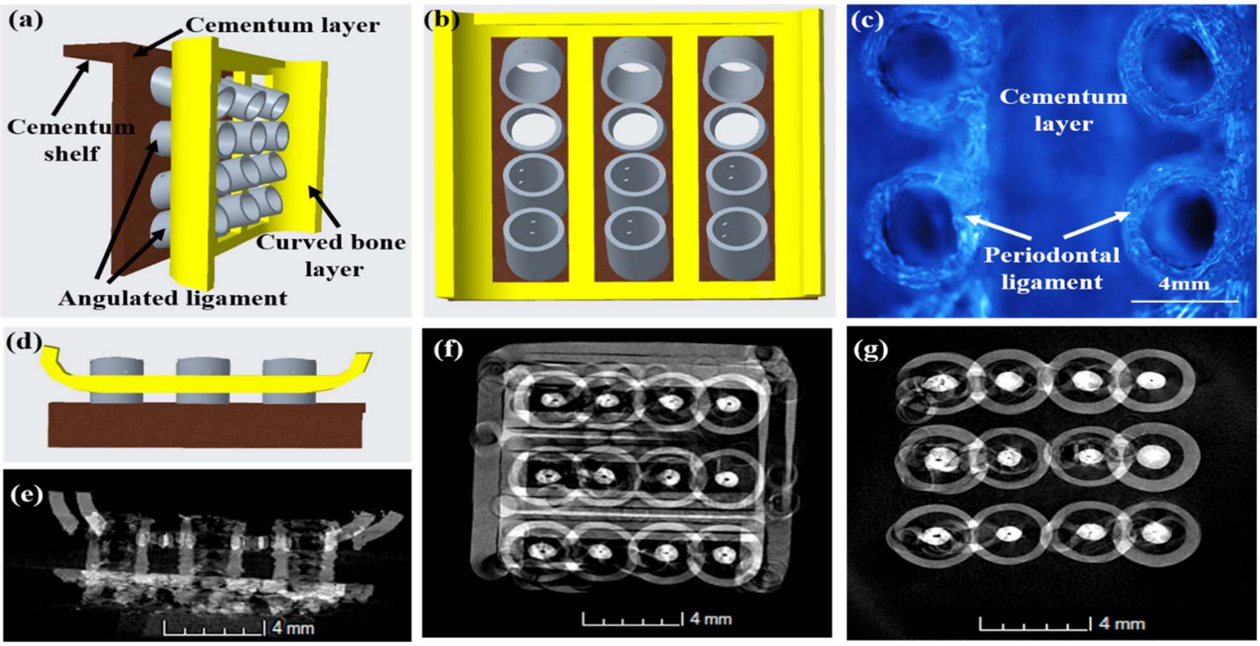

Fig. 3 3D model of the tri-layered scaffold (a) isometric view of the tri-layered scaffold (b) top view of the scaffold design showing the three distinct layers (c) optical image of the fabricated top surface of the ligaments which are attached on the cementum scaffold (d) side view of the scaffold model (e) side view of fabricated scaffold using micro-CT imaging (f) micro-CT image of cementum layer and ligaments interconnection (g) micro-CT image of the sliced periodontal ligament.

collagen formation. Fig. 3(b) shows the schematic of the scaffold design with three distinct layers. The periodontal tubes are given at various angles to replicate the periodontal ligament in the true periodontium structure, providing a lead for precise fiber formation and orientation, as shown in Fig. 3(a) and (b). Fig. 3(c) shows an optical microscopy image of the cementum layer and the periodontal ligament guiding tubes after fabrication using PLA material. Fig. 3(d) shows the schematic of the top side of the scaffold model, and the corresponding micro-CT image of the fabricated scaffold is shown in Fig. 3(e). To avoid the gingival epithelium moving lower (a typical issue after periodontal surgery that impairs the regeneration), the shelves (flat surface on cementum scaffold) on the scaffold have been designed to have a close adaptation to root or bone, as shown in Fig. 3(d). Fig. 3(f) shows a 3D reconstruction of the interconnection between the cementum layer and angulated ligaments using micro-CT imaging, and Fig. 3(g) shows the sliced part of the periodontal ligament using micro-CT imaging. The bone layer's curve aids in a perfect fit into the periodontal defect. To comprehend the microstructural composition of various layers, 1000 image frames at a 22 nm interspacing throughout the cross-section of the scaffold were used to reconstitute micro-CT scanning data sets as shown in Fig. 3(e)–(g).

Periodontal scaffolds are designed to interact closely with biological tissues, which include hard tissues like the bone and cementum, and soft tissues like the periodontal ligament. Tribological tests assess how these materials behave under mechanical stress, such as friction and wear, which is essential for ensuring compatibility and longevity within the oral environment. The coefficient of friction (COF) was plotted against the time for all the scaffolds, as shown in Fig. 4. PLA scaffolds on their own have a favorable coefficient of friction. GelMA coating on PLA is useful to deliver proteins and growth factors, and we observed a very ideal coefficient of friction for PLA/10 GelMA scaffold. PLA/10 GelMA had the lowest COF of 0.1198, followed by PLA scaffold with a COF of 0.1339. PLA/COL had a COF of 0.3218, and PLA/5 GelMA scaffold had a COF of 0.366. The increase in the frictional characteristics for PLA/COL and PLA/5 GelMA could be attributed to their relatively low surface roughness and mechanical properties compared to the PLA scaffold.[39]

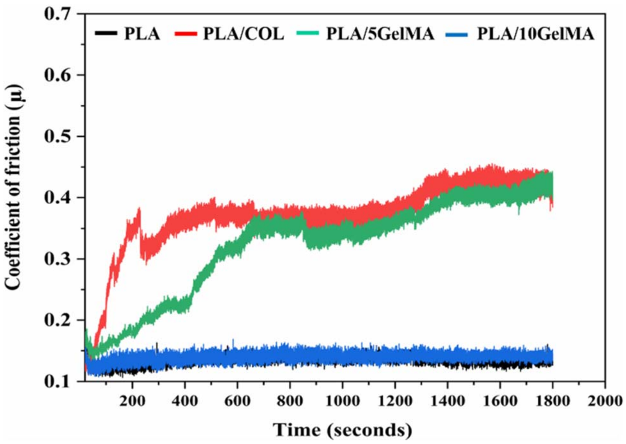

Fig. 4 Plot of coefficient of friction for PLA, PLA/COL, PLA/5 GelMA and PLA/10 GelMA scaffolds for time period from 0 seconds to 1800 seconds.

Cell-surface interactions are essential for the application of a biomaterial in tissue engineering. It is obvious that, in addition to the chemical composition of materials, the surface topography of a biomaterial affects cellular adhesion, migration, proliferation, and differentiation.[14] When developing scaffolds for tissue regeneration, surface roughness is an important factor to take into account because it has been demonstrated to affect cell adherence and proliferation in both 2D and 3D scaffolds.[40] The SEM experiment was performed to examine the surface morphology of the scaffold's individual layers. Moreover, the surface topography of the 3D printed devices depends on the design and the manufacturing process.[41] When compared to the various coated scaffolds used in our work, the PLA scaffold representing cementum, ligament, and bone layer has been shown to have a rough surface as in ESI Fig. S3(a)–(c).† The PLA/COL scaffold has a smoother surface topology, which might be attributed to the collagen entrapment on the PLA scaffold during the immersion process, as shown in Fig. S3(d)–(f)† for the cementum, ligament, and bone layer. Depending on the concentration of GelMA employed for the application, the inherent microstructure pores of GelMA can be tuned.[42] Higher concentrations of GelMA typically contain smaller interconnecting pores than lower concentrations of GelMA. For the PLA/5 GelMA cementum layer and on the periodontal ligaments linked to the scaffold, the larger pores are readily visible in Fig. S3(g)–(i).† The average pore size was found to be 54.823 ± 14.02 μm using ImageJ software. Larger pores allow for easier penetration of cells into the scaffold. Cells can infiltrate and adhere to the walls of the pores, promoting cell attachment and spreading. Pore size also directly affects the available surface area for cell adhesion.[43] Smaller pores provide a larger surface area per unit volume, which can enhance cell attachment as more cells can adhere to the surface.[29] Moreover, the pore size can influence the extent of interaction between cells, the gel matrix, and the scaffolds. Nutrient and oxygen diffusion through the pores are directly proportional to the pore size.[29] Mechanical properties are affected by changes in pore size. Changes in stiffness and elasticity can influence cell behavior, including adhesion and spreading.[43] For PLA/10 GelMA, the cementum and ligament surfaces exhibit a reduction in an average pore size by 50%. These observations were verified through SEM images, as shown in Fig. S3(j)–(l).†

The question arises if surface roughness is essential for cell adhesion and also whether this coating will interfere with cell adhesion or not. Bumgardner *et al.* showed coating chitosan on titanium reduced the contact angle and increased the adhesion of cells which attributed to increased protein adsorption and cell attachment.[44] It is highly possible for a similar process to happen in our study, and it is evident from high cellular proliferation. The average surface roughness (R_a) from the AFM study is depicted in Table 1.

It is clearly evident that the cementum and bone layer for the PLA scaffold have the highest surface roughness compared to

Table 1 Comparison of average surface roughness for PLA, PLA/COL, PLA/5 GelMA, and PLA/10 GelMA scaffolds by AFM. All data are reported as mean ± standard deviation ($n = 3$)

Group	Cementum scaffold roughness (nm)	Bone scaffold roughness (nm)
PLA	86.3 ± 10.81	61.06 ± 12.48
PLA/COL	56.53 ± 32.76	26.97 ± 1.59
PLA/5 GelMA	56.63 ± 22.16	37.43 ± 16.69
PLA/10 GelMA	44.87 ± 9.96	23.7 ± 6.07

the other PLA-coated scaffolds, such as PLA/COL, PLA/5 GelMA, and PLA/10 GelMA scaffold. C. N. Grover *et al.*[45] confirm that crosslinking reduces the surface roughness and reaffirms our finding for a reduced surface roughness for PLA/5 GelMA and PLA/10 GelMA when compared to PLA and PLA/COL scaffolds. This difference may be attributed to the porosity and pore size difference between the coatings PLA/5 GelMA and PLA/10 GelMA.[46] Fig. 5 shows the roughness variation of (a) PLA cementum layer (b) PLA bone layer (c) PLA/COL cementum layer (d) PLA/COL bone layer (e) PLA/5 GelMA cementum layer (f) PLA/5 GelMA bone layer (g) PLA/10 GelMA cementum layer and (h) PLA/10 GelMA bone layer. From these images, it is clear that for PLA scaffolds, surface roughness is higher than PLA/COL, PLA/5 GelMA, and PLA/10 GelMA. The Table S1 in ESI† depicts the Root mean square roughness (R_q) for all the scaffolds.

The PLA is a hydrophobic polymer due to the lack of reactive side-chain groups. The PLA cementum layer shows a contact angle of approximately 88°, thereby indicating a hydrophobic nature. Similarly, the change in the 3D printed structure affects the hydrophilicity,[46] and it can be seen from the contact angle variation for the PLA bone layer, which is approximately 82°. The wettability of the PLA layer rises when the layer is coated with collagen solutions, improving the scaffold's bioactivity. This is because the hydrophilic group's monomer that contains carboxyl, amide, and hydroxyl, present in glycine, proline, as well as hydroxyproline polypeptides have been introduced into the PLA backbone due to the presence of the collagen monomer. A contact angle of 40°–70° is ideal for cell adherence,[47] and we were able to achieve a contact angle of 70° in both PLA/COL and PLA/5 GelMA, making it appropriate for cell adhesion. The GelMA coatings have also decreased the hydrophobicity of the scaffold to 76° and 84° for PLA/5 GelMA and PLA/10 GelMA cementum layer. A similar trend follows for the bone layer as well.

Moreover, depending on the concentration of the GelMA, the contact angle can vary. For higher concentrations of GelMA, the contact angle increased in our work and is consistent with other works.[5] Fig. 6(a) shows the comparison of contact angle measurement with different coatings on cementum layer fabricated using PLA material. Fig. 6(b) shows the comparison of contact angle measurements for all the four types of bone layers fabricated using PLA material. Fig. S4 in ESI† shows the

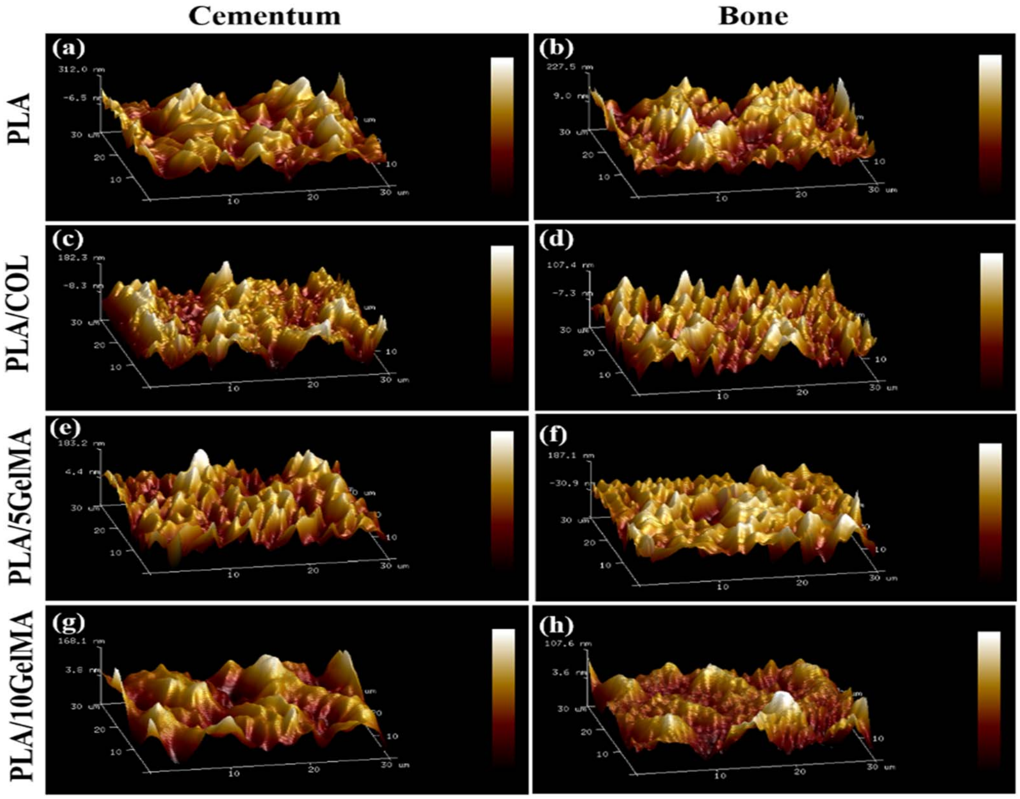

Fig. 5 AFM images of the scaffold. Roughness variation in (a) PLA cementum layer (b) PLA bone layer (c) PLA/COL cementum layer (d) PLA/COL bone layer (e) PLA/5 GelMA cementum layer (f) PLA/5 GelMA bone layer (g) PLA/10 GelMA cementum layer and (h) PLA/10 GelMA bone layer.

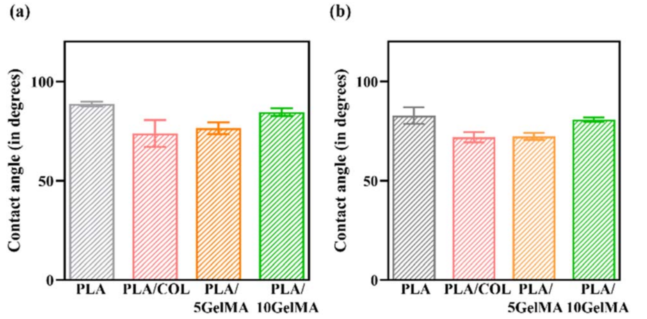

Fig. 6 Contact angle measurement (a) cementum layer for PLA, PLA/COL, PLA/5 GelMA and PLA/10 GelMA (b) bone layer for PLA, PLA/COL, PLA/5 GelMA and PLA/10 GelMA.

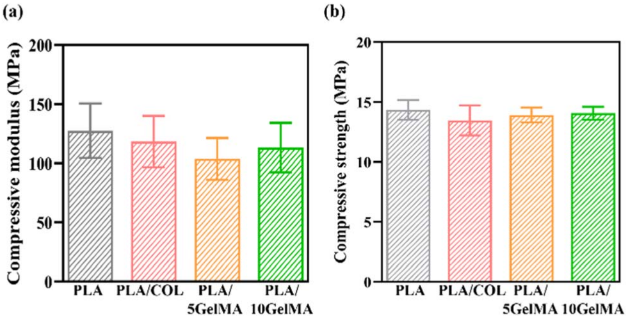

Fig. 8 Compression testing (a) compressive modulus for PLA, PLA/COL, PLA/5 GelMA and PLA/10 GelMA (b) compressive strength for PLA, PLA/COL, PLA/5 GelMA and PLA/10 GelMA.

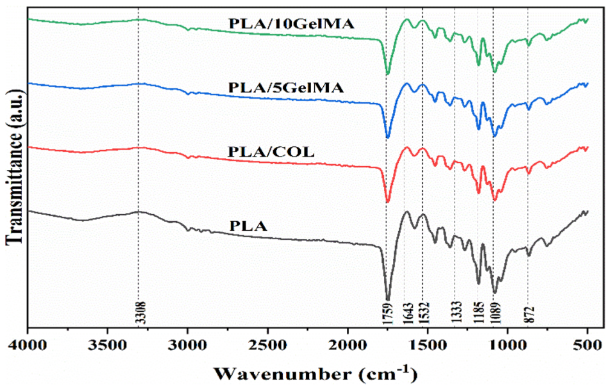

Fig. 7 The ATR-FTIR spectra indicating the functional groups present in PLA, PLA/COL, PLA/5 GelMA and PLA/10 GelMA. The significance bands for PLA, collagen and GelMA are indicated in the figure.

contact angle of the bone layer for PLA control scaffold, PLA/COL, PLA/5 GelMA, and PLA/10 GelMA scaffold. Fig. S5† in shows the contact angle for the cementum layer for PLA, PLA/COL, PLA/5 GelMA, and PLA/10 GelMA.

The material characterization of the PLA scaffold with different coating was performed using ATR-FTIR. Fig. 7 shows the ATR-FTIR spectra of the PLA scaffold showing distinctive absorption bands associated to the C═O stretch at 1759 cm^{-1} and the C–O–C stretching vibration at 1333 cm^{-1}. The backbone ester group of the PLA material is represented by the short bonds at 1185 cm^{-1} and 1089 cm^{-1}. The overlap of collagen monomer with the PLA backbone caused by the interaction of the NH_2 bond of the secondary amine with the PLA carbon chain is at 872 cm^{-1} for PLA/COL.[48] For GelMA coated samples, the amide I and the amide II band can be visualized at 1643 cm^{-1} and 1532 cm^{-1}.

3.2 Mechanical characterization

Compared to the other scaffolds, the PLA scaffold has demonstrated the highest compressive modulus of elasticity. The first elastic phase of the stress–strain curve was followed by a linear region with a lower slope, which is attributed to the progressive collapse of the macropores.[40] Although the force is inadequate to cause the structure to collapse, this behavior could be related to the deformation of the micropores.[40] The entrapment of collagen on the PLA scaffold has led to the lowering of the compressive modulus for PLA/COL, and here, collagen does not act as a reinforcement material but rather helps in cell adhesion and proliferation. This characteristic is similar to the other literatures.[18,49] When considering GelMA coating, similar effects like in the case of collagen are evident, although when GelMA concertation is increased, the compressive modulus has improved by a factor of 8.74%.[50] When comparing the compressive strength of the scaffolds, PLA has the highest compression strength of approximately 14.36 MPa, followed by PLA/10 GelMA with 14.085 MPa, then followed by PLA/5 GelMA and PLA/COL with 13.92 MPa and 13.48 MPa. Fig. 8(a) shows the comparison of compression modulus for different scaffolds such as PLA, PLA/COL, PLA/5 GelMA, and PLA/10 GelMA. Fig. 8(b) illustrates the comparison of compressive strength for different scaffolds such as PLA, PLA/COL, PLA/5 GelMA, and PLA/10 GelMA. Gauthier *et al.* proposed an opinion that not much significance has been given to the external load due to mastication and geometry of the tooth, which will deform the scaffolds unless the mechanical properties provide the necessary resistance.[14] Without the stiffness of the material and architecture, the scaffold may not provide the proper signal to the cells. Ben-Zvi *et al.*[51] and Jeannin *et al.*[52] concur with the previous authors and recommend scaffolds that can withstand masticatory forces. Previously, not much attention has been given to this important aspect in scaffold designing. In our scaffold design, there is a good compressive strength even under a force of 2010 N (normal masticatory load is 500 to 700 N), which is much higher than the highest masticatory force.[53] Moreover, as recommended by Gauthier *et al.*,[14] we have given a suitable curvature to the scaffold, which will provide parallel root geometry and uniform space for hard tissue formation. In addition, a comparative study by Hall *et al.* demonstrated a good strength and modulus of the thinnest PLA (0.6 mm) even without the incorporation of carbon or graphene[54,55] and whereas our fabricated scaffold is 0.6 mm in thickness with a completely different geometry, including a direction-oriented angulated structure. Moreover, for periodontal bone defects, the superficial gum tissue (gingiva) migrates down, encroaching on the root and bone surface, which needs to be height augmented, and there is a good possibility that PLA may fulfill that requirement. The softer periodontal ligament, stretched between two harder tissues, undergoes maximum strain during mastication. In animals, the modulus of elasticity of the ligament ranges between 1 and 10 MPa, which can go down to 0.15 MPa in a state of small deformation.[55] Conventional polymers used in tissue engineering normally will have a modulus of elasticity 100 MPa and hence may not be ideal for periodontal regeneration.[56] Based on the periodontal properties and biomechanics, it's been suggested that the biomaterial used should be anisotropic.[57] Thus, periodontal ligament properties should be anisotropic, similar to an oriented fibrous scaffold. Thus, it is suggested that a periodontal scaffold should be designed with an elastic modulus of 150 kPa for small deformations to 5 MPa in higher deformations.[58] Here, we have used PLA, which is anisotropic in nature,[59] but we need to reduce the modulus to make the scaffold more accurate for periodontal regeneration, and this work is our future scope of the study.

3.3 Cell adhesion and proliferation studies of the scaffold

Cell adhesion and proliferation were investigated to evaluate the biocompatibility of individual layers inside the scaffold. Using calcein AM and PI dye, the live and dead cell staining was carried out on the cells present in the scaffold. The PI dye is a cell impermeable dye and it stain the nucleus of dead cells and produce red fluorescence.[33,34]

The calcein AM is cell permeable dye and it can hydrolyse inside the cell and produce green fluorescence in live cells cytosol.[60] We have used MG63 cells as the model for the bone layer, and L929 cells were used for ligament and cementum areas respectively. Fig. 9(a) shows the live L929 cells spreading throughout the direction-oriented tunable ligament layer (represented as hollow channels, as demonstrated in Fig. 2 and 3). Fig. 9 and 10 shows cell adhesion in ligament, cementum, and bone structure using PLA and PLA/10 GelMA scaffold, and all the layers displayed excellent cell adhesion and growth for all the cell types. Fig. 9 shows live and healthy cells of L929 and MG63 on the surfaces of the ligament, cementum, and bone for a PLA scaffold after 24 hours of seeding. Fig. 9(a), (d) and (g), further confirm that the surface did not exhibit toxicity. The imaging of dead cells is shown in Fig. 9(b), (e) and (h), where the majority of the surface did not exhibit any dead cells. The merged images of both live and dead cells are shown in Fig. 9(c), (f) and (i), which also confirmed that the majority of the cells on all surfaces of the PLA scaffold are live by producing green fluorescent color. Similarly, Fig. 10 shows the live and dead cell imaging of L929 and MG63 cells on PLA/10 GelMA scaffold. Fig. 10(a), (d) and(g) show the living cells that are actively multiplying on the surface of the angulated ligament, cementum, and bone. These images demonstrate that the PLA scaffold's GelMA coating does not have a harmful effect on the cells. Fig. 10(b), (e) and (h) show minimum red fluorescence, indicating minimum cell death on the PLA/10 GelMA scaffold. Fig. 10(c), (f) and (i) indicate the combined images of both living

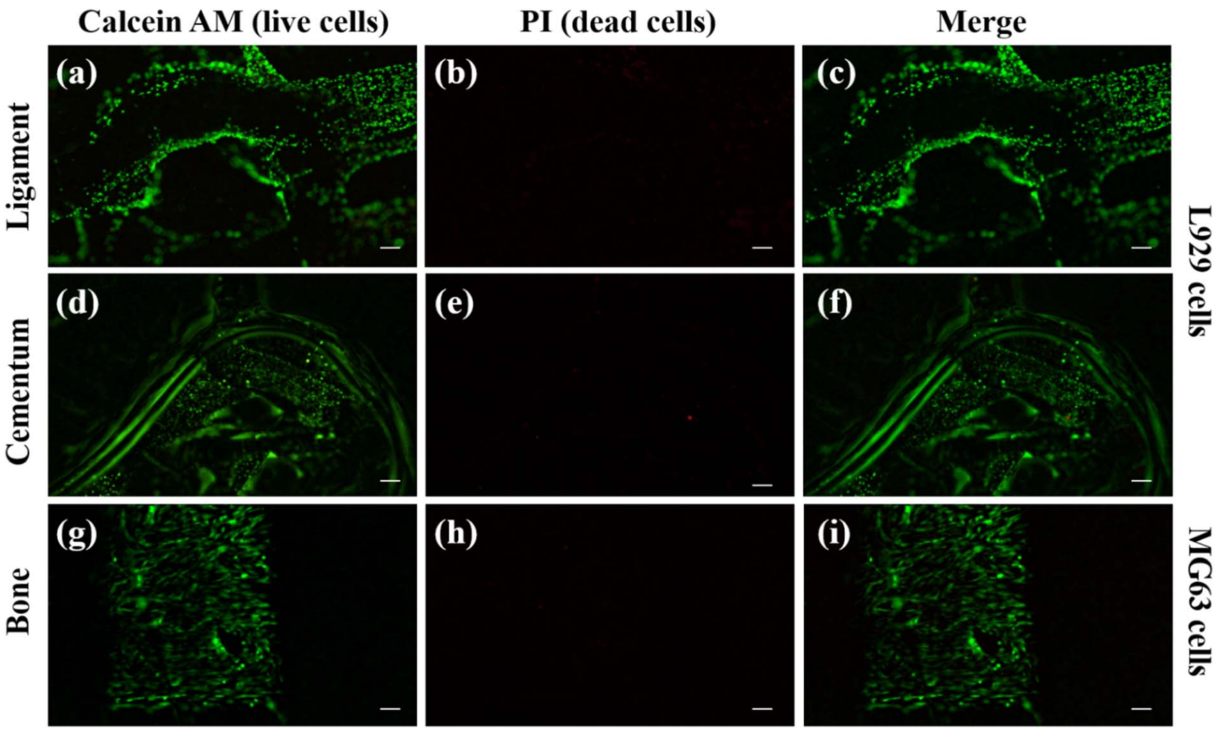

Fig. 9 Cell culture on PLA scaffold (a) live L929 cell staining on ligament layer using calcein AM (b) dead L929 cells staining on ligament layer using PI dye (c) merged image of live and dead cells (d) live L929 cell staining on cementum layer using calcein AM (e) dead L929 cells staining on cementum layer using PI dye (f) merged image of live and dead cells (g) live MG63 cell staining on bone layer using calcein AM (h) dead MG63 cells staining on bone layer using PI dye (i) merged image of live and dead cells. Scale for all images is 200 μm.

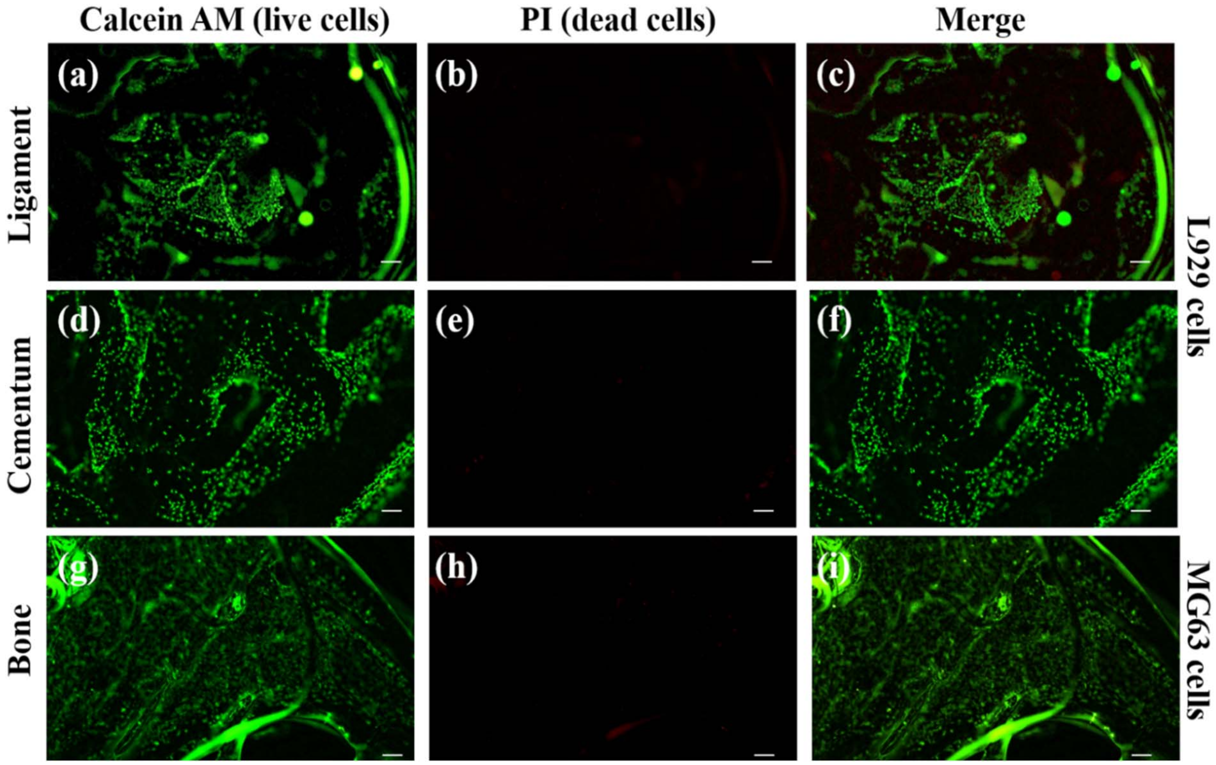

Fig. 10 Cell culture on PLA/10 GelMA scaffold (a) live L929 cell staining on ligament layer using calcein AM (b) dead L929 cells staining on ligament layer using PI dye (c) merged image of live and dead cells (d) live L929 cell staining on cementum layer using calcein AM (e) dead L929 cells staining on cementum layer using PI dye (f) merged image of live and dead cells (g) live MG63 cell staining on bone layer using calcein AM (h) dead MG63 cells staining on bone layer using PI dye (i) merged image of live and dead cells. Scale for all images is 200 μm.

and dead cells, which further demonstrated that the majority of the cells on the scaffold's surfaces are alive by creating green fluorescent colour.

Fig. S6 in ESI† shows the live and dead cells imaging on PLA/COL scaffold, Fig. S7† shows the live and dead cell cells imaging on PLA/5 GelMA scaffold. For Fig. 9, 10, S6, and S7† show that most of the cells live in ligament, cementum, and bone structure using different scaffold materials. Fig. S8† shows the L929 cells growing inside the ligament. The Fig. S8(a)–(h)† are taken at different depth. Fig. S9† shows the stacked images of cells inside the ligament for a PLA/5 GelMA scaffold. Fig. S10† shows live L929 cells on the cementum shelf and on the attached cementum surface for a PLA scaffold.

To understand the cell morphology on the scaffold, L929 cells were cultured on the scaffolds for 48 hours, and SEM images were taken. Fig. 11 shows the SEM images of L929 cells proliferating on the scaffolds. Fig. 11(a–c) indicates the cells on PLA scaffolds in different magnifications. Fig. 11(d–f) shows the cells on PLA/COL scaffolds. The elongated and flattened structure of the cells on the scaffold can be attributed to the stiffness of the scaffolds. Fig. 11(g–i) shows the enhanced cell adhesion and proliferation on the PLA/5 GelMA scaffold. Fig. 11(j–l) shows the interconnected cells thriving on PLA/10 GelMA scaffold. The SEM results showed good adhesion, migration, and proliferation of L929 cells on all the scaffolds, indicating that the cells can grow homogenously across the scaffold with effective cell–scaffold interactions. The cells on the control PLA scaffold tend to have lesser inter-cellular interaction, whereas, in the coated scaffolds, the cells seem to have spread more and tend to take an elongated shape.[61] This spreading or elongation indicates how cells adapt to the stiffness of their environment. This adaptation is part of the mechanotransduction process, where cells convert mechanical cues from the ECM into biochemical signals that influence cell behavior.[61] It can be seen that the cells form an interconnected structure on the GelMA-coated scaffolds. It can be inferred that the GelMA coating not only improved the scaffold's surface properties but also enhanced cell attachment and spreading, which are critical for tissue integration and regeneration applications.

3.4 Mineralization on bone layer

The ability of cells to produce a mineralized matrix is important for the development of materials suitable for bone regeneration. Alizarin Red S staining is commonly used to detect calcium deposits in mineralized tissues. Fig. S11† shows the images of the different bone layers stained with Alizarin red S after MG63 cells were cultured for 7 days. It can be clearly observed that a lightly stained surface was found on the scaffolds cultured in DMEM media, whereas more calcium nodules were formed on the same scaffolds cultured in osteogenic media. Furthermore, cells cultured on PLA/5 GelMA and PLA/10 GelMA revealed more intense calcification than the other groups. Quantification of

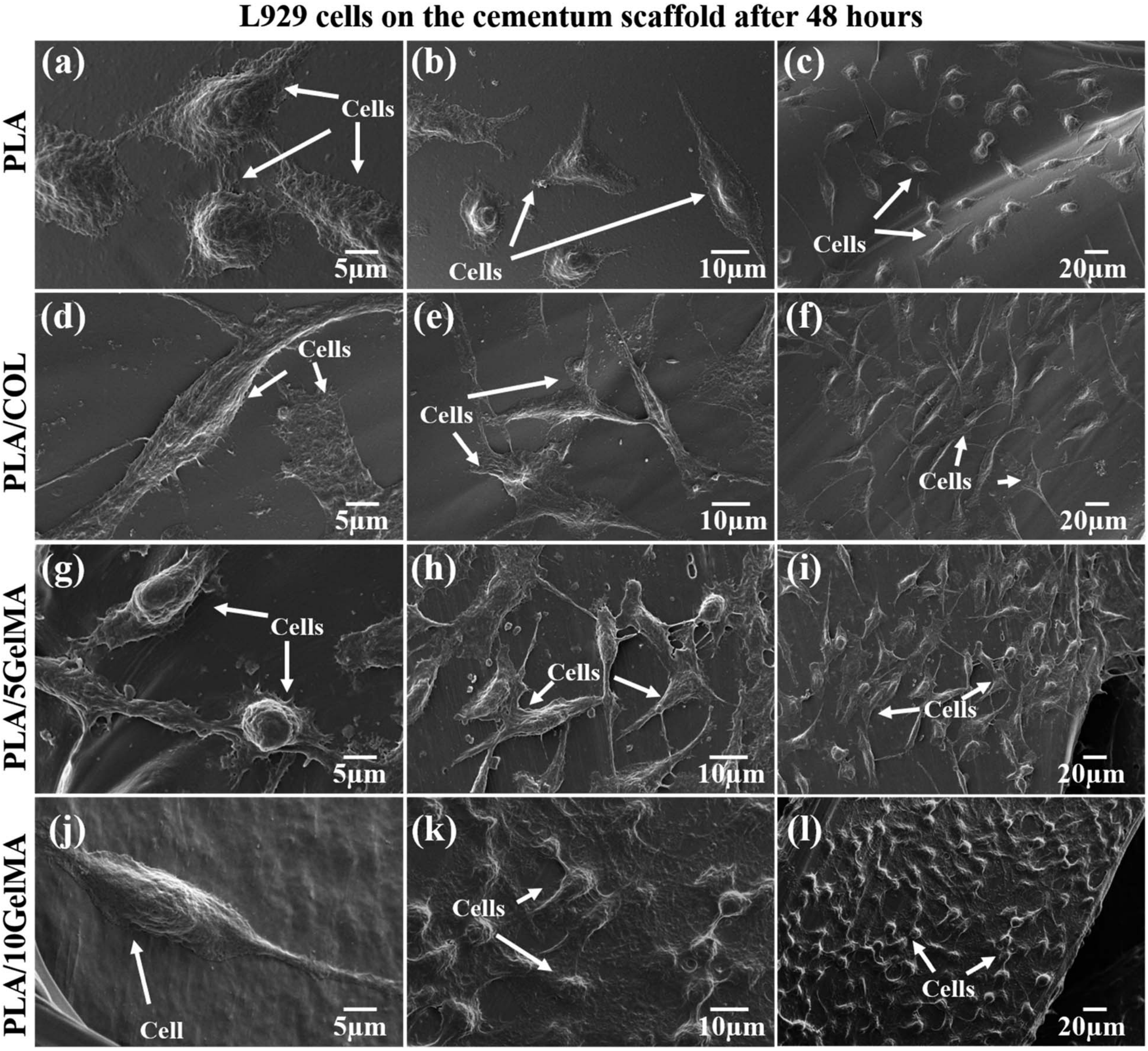

Fig. 11 SEM images of cell morphologies on scaffolds when the L929 cells had been cultured for 48 hours. (a,b,c) Shows cells on the control PLA scaffold. (d,e,f) Illustrate the relatively interconnected cells proliferating on PLA/COL cementum layers. (g,h,i) Indicate the elongated and highly interconnected cells on the surface of PLA/5 GelMA cementum layer. (j,k,l) Shows L929 cells elongated and thriving on the surface of PLA/10 GelMA cementum layers.

calcium mineral deposits by the Alizarin Red S assay is shown in Fig. 12.

It is clear from the graph that the calcium deposition increased with using osteogenic media than DMEM. More importantly, the calcium contents in PLA/5 GelMA and PLA/10 GelMA cultured in osteogenic media were significantly ($p <$ 0.0001) higher than those cultured in DMEM over 7 days. Similar improvement was also seen for the cells cultured on PLA/COL scaffolds in osteogenic media. No significant differences were present for MG63 cells cultured on PLA scaffolds in both mediums. It has been established that PLA/5 GelMA and PLA/10 GelMA coating exhibit good biocompatibility and are useful for improving the cell adhesion, proliferation, and viability on PLA 3D printed scaffolds.

3.5 *In vitro* wound closure assay

The *in vitro* wound closure assay can be used to understand the effect of scaffold materials in accelerating or decelerating the healing of wounds *in vitro*. The results obtained using the scratch test are given in Fig. S12.† The well without a scaffold serves as the control for the experiment. Fig. S12(a)† shows the initial cell-free area after the scratch (time 0 hours). Fig. S12(f), (k), (p) and (u)† indicates the cell migration into the scratched area after 12 hours, 24 hours, 48 hours, and 72 hours for the control. Fig. S12(b)–(e)† shows the initial scratch area before immersion of PLA, PLA/COL, PLA/5 GelMa and PLA/10 GelMA scaffolds respectively. After 12 h of treatment with the PLA scaffold, about 24% of the scratched area was healed in control due to the migration of L929 cells into the scratched

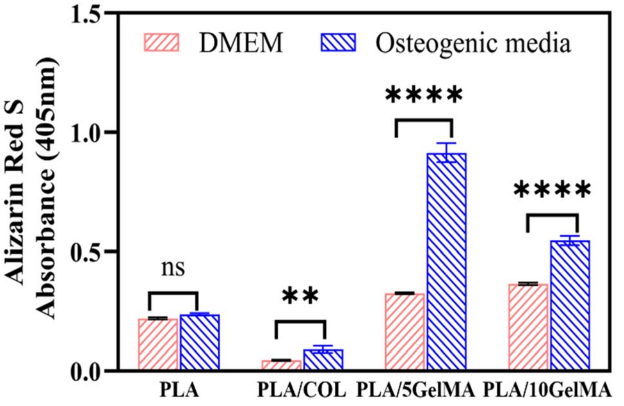

Fig. 12 Mineralization on scaffolds cultured in DMEM and osteogenic media. Statistical analysis is shown on the bar graphs. Data are presented as the mean and SD of the three independent experiments. $^{*}P < 0.0332$, $^{**}P < 0.0021$, $^{***}P < 0.0002$, and $^{****}P < 0.0001$.

area. Whereas, for PLA/COL, PLA/5 GelMA, and PLA/10 GelMA, the cell migration was limited to 8% to 19% after 12 hours, as shown in Fig. S12(g)–(j).† After 24 hours, PLA and PLA/10 GelMA scaffolds had almost 50% cell migration, followed by PLA/5 GelMA, PLA/COL, and control. After 48 hours, PLA/10 GelMA and PLA/5 GelMA had almost 90% cell migration, which was followed by PLA/COL, PLA, and control. A similar trend followed after 72 hours with 100% wound closure for PLA/10 GelMA and PLA/5 GelMA. The quantitative analysis of the cell migration is shown in Fig. 13. No significant differences were present for L929 cells cultured on all the scaffolds after 12 hours. After 24 hours, significant differences were present for PLA, PLA/COL, and PLA/10 GelMA scaffolds when compared to control. Subsequently, after 48 hours, a significant difference was observed for PLA/5 GelMA ($P < 0.0001$). After 72 hours, a significant difference was found for PLA/5 GelMA and PLA/10 GelMA scaffolds ($P < 0.0002$). Overall, it has been observed that PLA/COL, PLA/5 GelMA, and PLA/10 GelMA improved the cell migration for the *in vitro* wound model.

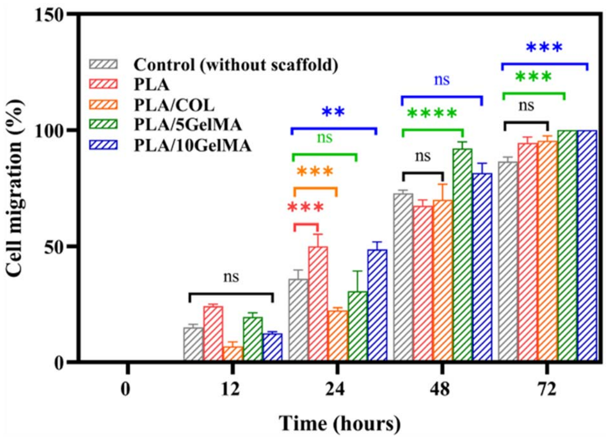

Fig. 13 Quantitative analysis of *in vitro* wound closure expressed as the area covered by the L929 cells. Data are presented as the mean and SD of the three independent experiments. $^{*}P < 0.0332$, $^{**}P < 0.0021$, $^{***}P < 0.0002$, and $^{****}P < 0.0001$.

3.6 MTT assay

Cytotoxicity test was performed using MTT (3-(4,5-dimethylthiazol)-2,5-diphenyl-tetrazolium bromide) assay. The cytotoxicity levels of the scaffolds were analyzed on days 1, 2, and 3 after the initial cell seeding. The trypsinized cells were seeded onto the respective sterilized scaffolds and allowed to incubate for an hour. After that, sufficient media was added to each well. On days 1, 2, and 3, a 10 µl of MTT reactant was introduced in DMEM cell culture medium followed by a four-hour incubation at 37 °C with 5% CO_2. After the incubation time, 100 µl DMSO was added, and then the solution was used for further studies. The quantity of formazan is measured by recording changes in absorbance at 570 nm using a plate reading spectrophotometer. The MTT assay indicates that the scaffolds maintain excellent cell viability in addition to serving as a cell adherent substrate as shown in Fig. 14. Fig. 14(a) indicates the plot of cell viability (%) against the number of days of culture for L929 cells and Fig. 14(b) shows the plot of cell viability (%) against number of days in culture for MG63 cells. Considering L929 cells, there were no significant changes between the control (without scaffold), PLA, and PLA/COL on day 1. Statistically significant differences in cell viability were observed on PLA/5 GelMA and PLA/10 GelMA ($p < 0.0002$ and $p < 0.0001$). On day 2, all scaffolds except PLA/10 GelMA had significant improvements in cell viability when compared to the control. On the third day, all the scaffolds had a significant increase in cell viability ($p < 0.0001$). As the days increased, it showed that cell viability was increasing continuously on all the scaffolds. On the PLA/5 GelMA and PLA/10 GelMA, the proliferation rate of the L929 cells is higher than that on the other scaffolds, and a similar increase was illustrated for the control experiment.

The proliferation of MG63 cells on day 1 had no significant changes for PLA/COL and PLA/5 GelMA when compared to the control. Whereas significant changes were noted for PLA and PLA/5 GelMA scaffolds. On the second day all the groups had no significant changes when compared to the control. A significant increase in cell viability was noted for all the scaffolds when compared to the control ($p < 0.0001$) on the third day. These data confirm the excellent biocompatibility of the scaffolds for tissue regenerative applications.

3.7 Flow cytometry

The quantitative analysis of the number of live and dead cell adherence on different scaffolds was performed using flow cytometry. After live and dead cells were stained on the scaffold by using calcein AM and PI dye, the cells were released by using trypsin and then centrifuged to obtain the cell pellet. Then the cells were tested using flow cytometry. The results show that cell viability is 100% for all types of scaffolds (PLA, PLA/COL, PLA/5 GelMA, and PLA/10 GelMA) using L929 and MG63 cell lines. This validates that the scaffolds are highly biocompatible. Fig. 15 shows the graph indicating the flow cytometry-based

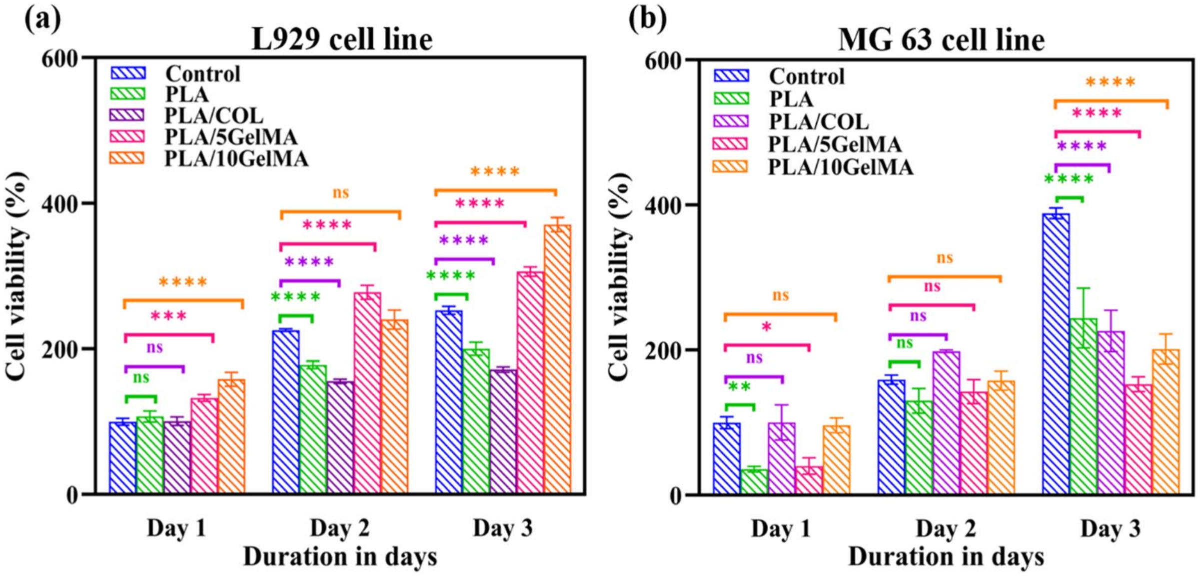

Fig. 14 The MTT assay test results showing the viability of (a) L929 cells on control, PLA scaffold, PLA/COL scaffold, PLA/5 GelMA scaffold and PLA/10 GelMA scaffold (b) MG63 cells in control, PLA scaffold, PLA/COL scaffold, PLA/5 GelMA scaffold and PLA/10 GelMA scaffold after 1, 2, and 3 days of incubation. Statistical analysis was performed using two-way ANOVA test. Statistical significance was assumed for p-values (*$p < 0.0332$, **$p < 0.0021$, ***$p < 0.0002$, and ****$p < 0.0001$).

quantification of live and dead L929 cells on the different types of scaffolds. Fig. 15(a) shows the unstained cell population used for the experiment. Fig. 15(b) indicates the cells stained red using PI dye. Fig. 15(c) indicates the live cells stained using calcein AM dye. Fig. 15(d)–(g) illustrates the live and dead cell populations on the PLA, PLA/COL, PLA/5 GelMA, and PLA/10 GelMA scaffolds. It clearly indicates that 100% of L9292 cells are viable on the scaffolds. A similar analysis for MG63 cell lines

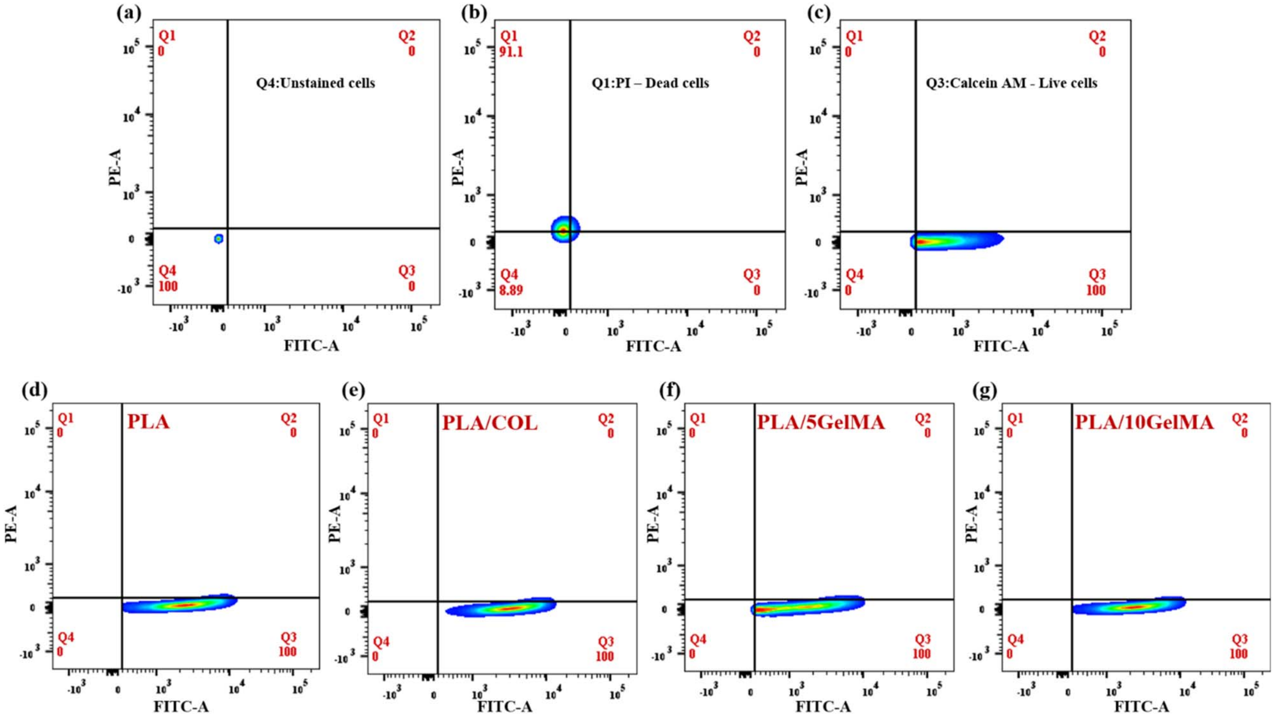

Fig. 15 Flow cytometry-based quantification of live and dead L929 cells on scaffolds. (a) Unstained L929 cell population (b) cell stained with PI dye (dead cells) (c) cells stained with calcein AM (live cells) (d) the percentage of live and dead cells on PLA scaffold (e) the percentage of live and dead cells on PLA/COL scaffold (f) the percentage of live and dead cells on 5 GelMA scaffold (g) the percentage of live and dead cells on PLA/10 GelMA scaffold after 1 day incubation.

was done on all the scaffolds. The images have been included in Fig. S13 in ESI.† From the figure, it is demonstrated that 100% of MG63 cells are viable on all the scaffolds. Culturing fibroblast and osteoblast cells on the scaffold exhibit high cell viability, and both cell types are attached to all four types of scaffolds (uncoated and coated). The cells looked healthy, and the more interesting point is that the cell attached to the inner surface of the angulated bars, that is, the inner side of the direction-oriented ligament layer, as shown in Fig. S8.† Hence, all four types of scaffolds are non-cytotoxic and have excellent biocompatibility. Moreover, flow cytometry analysis showed a yield of 100% viable cells for all the scaffolds. The presence of both fibroblasts and osteoblasts makes this scaffold suitable for periodontal regeneration. A detailed comparison between our work and similar work has been included in ESI as Table S2.†

While this *in vitro* study provides valuable insights into the efficacy of the 3D-printed tri-layered scaffold in promoting periodontal regeneration, in the future, we plan to miniaturize the size of the scaffold using PLA and PCL biomaterials and explore the avenues for translation of scaffold-based therapies from preclinical models to clinical applications. This scaffold has been designed taking into consideration the real-time periodontal defect.

4 Conclusions

For the first time, a three-layered, biocompatible PLA polymer scaffold for periodontal regeneration is proposed, where direction-oriented tunable ligament fiber can be grown in between cementum and bone layer, and it can be customised in the future with different scaffold volume requirements from patient to patient. The periodontium's natural structure is not accurately represented to date. In the natural periodontium condition, the periodontal ligament fibers can be found in four various orientations along the tooth's root: crystal, horizontal, oblique, and apical. In our work, we printed alveolar bone, periodontal ligament, and cementum using PLA material coated with collagen as well as different concentrations of GelMA to improve the biocompatibility, surface, and mechanical properties of the scaffold. The advantage of our novel design is a movable 3D scaffold over any stationary scaffold, and it can be completely customized to fit any type of periodontal deformity; moreover, it provides guidance for the cell to accumulate and form the periodontal ligament. The length of the periodontal ligament can be changed by clipping the ends of the tubes to match the anatomy of the defect. The scaffold additionally offers cell compartmentalization by the incorporation of different layers and anchorage between the ligament and bone. Moreover, the scaffolds offer a great degree of functionalization. Therefore, it is a promising approach for personalized tissue engineering applications.

Author contributions

Conceptualization: SR, TSS. Methodology: SA, PG, KG, SR, TSS. Investigation: SA. Device fabrication SA, PG. Schematics: TSS. Data analysis: SA, SR, TSS. Supervision: TSS. Resources: TSS. Writing – original draft: SA, KG, SR. Writing – review & editing: KG, SR, TSS.

Conflicts of interest

There are no conflicts to declare.

Acknowledgements

We gratefully acknowledge the partial financial support provided by Science and Engineering Research Board (SERB), India, under grant number CRG/2022/003167. We are thankful for the fabrication support received from Dr G. Saravana Kumar and Mr Socratees S. (Dept. of Engineering Design, IITM, India). We would also like to thank the help provided by Dr R. Srividhya for Flow Cytometry facility (Bio-SAIF, Dept. of Biotechnology, IITM, India). We also take this opportunity to thank Dr Vignesh Muthuvijayan and Dr Shanthanu Pradhan (Dept. of Biotechnology, IITM, India) for the support received during the GelMA synthesis. We are thankful to Dr R. Sarathi (Dept. of Electrical Engineering, IITM, India) for the support received during AFM characterization, Dr Ramkumar P. and Dr Krishnan Balasubramaniam (Dept. of Mechanical Engineering, IITM, India) for all the assistance provided for the tribological studies and micro CT imaging. In addition, we would like to thank Dr R. Jayaganthan (Dept. of Engineering Design, IITM, India) and Dr Pijush Ghosh (Dept. of Applied Mechanics & Biomedical Engineering, IITM, India) for their help in conducting the compression testing for the scaffolds. We also take this opportunity to thank Dr Srabani Kar (IISER, Tirupati, India) for drawing the schematic for this manuscript. We would like to thank Mr Suhridh Sundaram (Avay Biosciences Pvt. Ltd, Karnataka, India) for the support received during designing the scaffold.

References

1 T. de Jong, A. D. Bakker, V. Everts and T. H. Smit, *J. Periodontal Res.*, 2017, **52**, 965–974.
2 T. Larsen and N. E. Fiehn, *Apmis*, 2017, **125**, 376–384.
3 M. Nazir, A. Al-Ansari, K. Al-Khalifa, M. Alhareky, B. Gaffar and K. Almas, *Sci. World J.*, 2020, **2020**, 2146160.
4 J. Kim and S. Amar, *Odontology*, 2006, **94**, 10–21.
5 Y. Liang, X. Luan and X. Liu, *Bioact. Mater.*, 2020, **5**, 297–308.
6 H. N. Woo, Y. J. Cho, S. Tarafder and C. H. Lee, *Bioact. Mater.*, 2021, **6**, 3328–3342.
7 D. Fraser, J. Caton and D. S. W. Benoit, *Front. Dent. Med.*, 2022, **3**, 1–24.
8 S. Sowmya, U. Mony, P. Jayachandran, S. Reshma, R. A. Kumar, H. Arzate, S. V. Nair and R. Jayakumar, *Adv. Healthcare Mater.*, 2017, **6**, 1–13.
9 T. Ding, J. Li, X. Zhang, L. Du, Y. Li, D. Li, B. Kong and S. Ge, *Biomater. Sci.*, 2020, **8**, 2459–2471.
10 M. T. Vurat, Ş. Şeker, Ö. Lalegül-Ülker, M. Parmaksiz, A. E. Elçin and Y. M. Elçin, *Genes Dis.*, 2022, **9**, 1008–1023.

11 D. G. Miranda, S. M. Malmonge, D. M. Campos, N. G. Attik, B. Grosgogeat and K. Gritsch, *J. Biomed. Mater. Res., Part B*, 2016, **104**, 1691–1702.

12 Y. Guo, X. Jiang, P. Pan, X. Liu, L. Huang, M. Li and Y. Liu, *Int. J. Polym. Mater. Polym. Biomater.*, 2022, **72**, 1445–1454.

13 N. Abedi, N. Rajabi, M. Kharaziha, F. Nejatidanesh and L. Tayebi, *J. Oral Biol. Craniofac. Res.*, 2022, **12**, 782–797.

14 R. Gauthier, C. Jeannin, N. Attik, A. M. Trunfio-Sfarghiu, K. Gritsch and B. Grosgogeat, *J. Biomech. Eng.*, 2021, **143**, 1–13.

15 C. H. Lee, J. Hajibandeh, T. Suzuki, A. Fan, P. Shang and J. J. Mao, *Tissue Eng., Part A*, 2014, **20**, 1342–1351.

16 Y. Yao, J. E. Raymond, F. Kauffmann, S. Maekawa, J. V. Sugai, J. Lahann and W. V. Giannobile, *J. Dent. Res.*, 2022, **101**, 1457–1466.

17 S. Pitaru, H. Tal, M. Soldinger and M. Noff, *J. Periodontal Res.*, 1989, **24**, 247–253.

18 C. H. Park, K. H. Kim, Y. M. Lee, W. V. Giannobile and Y. J. Seol, *Int. J. Mol. Sci.*, 2017, **18**(9), 1927.

19 M. S. A. Hamzah, C. Ng, N. I. S. Zulkarnain, H. A. Majid, S. I. A. Razak and N. H. M. Nayan, *Mater. Today: Proc.*, 2020, **46**, 1668–1673.

20 A. Daghrery and M. C. Bottino, *Genesis*, 2022, **60**, 1–13.

21 M. P. Dieterle, T. Steinberg, P. Tomakidi, J. Nohava, K. Vach, S. D. Schulz, E. Hellwig and S. Proksch, *Pharmaceutics*, 2022, **14**, 1–27.

22 D. Tadic and M. Epple, *Biomaterials*, 2004, **25**, 987–994.

23 H. Fan, C. Zhang, J. Li, L. Bi, L. Qin, H. Wu and Y. Hu, *Biomacromolecules*, 2008, **9**, 927–934.

24 R. J. Staples, S. Ivanovski and C. Vaquette, *J. Periodontal Res.*, 2020, **55**, 331–341.

25 C. V. Reuben Staples, S. Ivanovski and K. Vaswani, *Acta Biomater.*, 2024, **180**, 337–357.

26 M. A. Sakr, M. G. A. Mohamed, R. Wu, S. Ryon and D. Kim, *Appl. Clay Sci.*, 2020, **199**, 105860.

27 B. D. Fairbanks, M. P. Schwartz, C. N. Bowman and K. S. Anseth, *Biomaterials*, 2009, **30**, 6702–6707.

28 N. Monteiro, W. He, C. M. Franca, A. Athirasala and L. E. Bertassoni, *ACS Biomater. Sci. Eng.*, 2018, **4**, 2563–2570.

29 J. He, Y. Sun, Q. Gao, C. He, K. Yao, T. Wang, M. Xie, K. Yu, J. Nie, Y. Chen and Y. He, *Adv. Healthcare Mater.*, 2023, **12**, 1–24.

30 N. Rodrigues, M. Benning, A. M. Ferreira, L. Dixon and K. Dalgarno, *Procedia CIRP*, 2016, **49**, 33–38.

31 C. Ruiz, M. Vera, B. L. Rivas, S. Sánchez and B. F. Urbano, *RSC Adv.*, 2020, **10**, 43799–43810.

32 D. Loessner, C. Meinert, E. Kaemmerer, L. C. Martine, K. Yue, P. A. Levett, T. J. Klein, F. P. W. Melchels, A. Khademhosseini and D. W. Hutmacher, *Nat. Protoc.*, 2016, **11**, 727–746.

33 P. Gupta, S. Waghmare, S. Kar, K. Illath, S. Rao and T. S. Santra, *RSC Adv.*, 2023, **13**, 1245–1255.

34 A. Shinde, P. Shinde, S. Kar, K. Illath, S. Dey, N. R. Mahapatra, M. Nagai and T. S. Santra, *Lab Chip*, 2023, **23**, 2175–2192.

35 C. C. Ho and S. J. Ding, *J. Mater. Chem. B*, 2015, **3**, 2698–2707.

36 M. P. Bernardo, B. C. R. da Silva, A. E. I. Hamouda, M. A. S. de Toledo, C. Schalla, S. Rütten, R. Goetzke, L. H. C. Mattoso, M. Zenke and A. Sechi, *Sci. Rep.*, 2022, **12**, 1–15.

37 B. N. Brown, C. A. Barnes, R. T. Kasick, R. Michel, T. W. Gilbert, D. Beer-Stolz, D. G. Castner, B. D. Ratner and S. F. Badylak, *Biomaterials*, 2010, **31**, 428–437.

38 A. Abdul Samat, Z. A. Abdul Hamid, M. Jaafar, C. C. Ong and B. H. Yahaya, *Bioengineering*, 2023, **10**(4), 394.

39 C. L. Kim and D. E. Kim, *Sci. Rep.*, 2016, **6**, 1–11.

40 A. R. Calore, V. Srinivas, L. Groenendijk, A. Serafim, I. C. Stancu, A. Wilbers, N. Leoné, A. A. Sanchez, D. Auhl, C. Mota, K. Bernaerts, J. A. W. Harings and L. Moroni, *Acta Biomater.*, 2023, **156**, 158–176.

41 Y. Quinsat, C. Lartigue, C. A. Brown and L. Hattali, *Int. J. Interact. Des. Manuf.*, 2018, **12**, 1007–1014.

42 L. Luo, Y. He, L. Jin, Y. Zhang, F. P. Guastaldi, A. A. Albashari, F. Hu, X. Wang, L. Wang, J. Xiao, L. Li, J. Wang, A. Higuchi and Q. Ye, *Bioact. Mater.*, 2021, **6**, 638–654.

43 K. Yue, G. Trujillo-de Santiago, M. M. Alvarez, A. Tamayol, N. Annabi and A. Khademhosseini, *Biomaterials*, 2015, **73**, 254–271.

44 J. D. Bumgardner, B. M. Chesnutt, Y. Yuan, Y. Yang, M. Appleford, S. Oh, R. Mclaughlin, S. H. Elder and J. L. Ong, *Implant Dent.*, 2007, **16**, 66–79.

45 C. N. Grover, J. H. Gwynne, N. Pugh, S. Hamaia, R. W. Farndale, S. M. Best and R. E. Cameron, *Acta Biomater.*, 2012, **8**, 3080–3090.

46 F. Jahanmard, A. Khodaei, J. Flapper, O. Dogan, K. Roohi, P. Taheri, H. Weinans, G. Storm, M. Croes, E. Mastrobattista and S. Amin Yavari, *J. Controlled Release*, 2023, **358**, 667–680.

47 Y. J. Chuah, Y. T. Koh, K. Lim, N. V. Menon, Y. Wu and Y. Kang, *Sci. Rep.*, 2015, **5**, 1–12.

48 Y. He, W. Liu, L. Guan, J. Chen, L. Duan, Z. Jia, J. Huang, W. Li, J. Liu, J. Xiong, L. Liu and D. Wang, *BioMed Res. Int.*, 2018, **2018**, 5147156.

49 B. Ashwin, B. Abinaya, T. P. Prasith, S. V. Chandran, L. R. Yadav, M. Vairamani, S. Patil and N. Selvamurugan, *Int. J. Biol. Macromol.*, 2020, **162**, 523–532.

50 H. J. Yoon, S. R. Shin, J. M. Cha, S. H. Lee, J. H. Kim, J. T. Do, H. Song and H. Bae, *PLoS One*, 2016, **11**, 1–18.

51 Y. Ben-Zvi, R. Maria, M. Pierantoni, V. Brumfeld, R. Shahar and S. Weiner, *J. Struct. Biol.*, 2019, **205**, 155–162.

52 C. Jeannin, K. Gritsch, J. J. Liodénot and B. Grosgogeat, *Comput. Methods Biomech. Biomed. Eng.*, 2019, **22**, S62–S64.

53 S. S. Kumararama and R. Chowdhary, *Indian J. Dent. Res.*, 2017, **28**, 309–313.

54 M. S. Hall, R. Long, C. Y. Hui and M. Wu, *Biophys. J.*, 2012, **102**, 2241–2250.

55 M. Pini, P. Zysset, J. Botsis and R. Contro, *J. Biomech.*, 2004, **37**, 111–119.

56 M. N. Taravel and A. Domard, *Biomaterials*, 1996, **17**, 451–455.

57 R. Deng, Y. Xie, U. Chan, T. Xu and Y. Huang, *J. Dent. Res. Dent. Clin. Dent. Prospects*, 2022, **16**, 1–10.

58 N. Yoshida, Y. Koga, C. L. Peng, E. Tanaka and K. Kobayashi, *Med. Eng. Phys.*, 2001, **23**, 567–572.

59 L. C. Mozdzen, A. Vucetic and B. A. C. Harley, *J. Mech. Behav. Biomed. Mater.*, 2017, **66**, 28–36.

60 K. Illath, A. Shinde, P. Paremmal, P. Gupta, M. Nagai and T. S. Santra, *Surf. Interfaces*, 2023, **36**, 102478.

61 J. K. Kular, S. Basu and R. I. Sharma, *J. Tissue Eng.*, 2014, **5**, 2041731414557112.